



Synergistic engineering of heteronuclear Ni-Ag dual-atom catalysts for high-efficiency CO₂ electroreduction with nearly 100% CO selectivity

Zeyu Guo^{a,b}, Huiwen Zhu^{a,b}, Gang Yang^{a,b}, Angjian Wu^c, Quhan Chen^{a,b}, Zijun Yan^{a,b}, Kam Loon Fow^{a,b}, Hainam Do^{a,b}, Jonathan D. Hirst^d, Tao Wu^{a,b,*}, Mengxia Xu^{a,b,*}

^a Department of Chemical and Environmental Engineering, and New Materials Institute, University of Nottingham Ningbo China, Ningbo 315100, China

^b Key Laboratory of Carbonaceous Waste Processing and Process Intensification of Zhejiang Province, University of Nottingham Ningbo China, Ningbo 315100, China

^c State Key Laboratory of Clean Energy Utilization, Department of Energy Engineering, Zhejiang University, Hangzhou 310027, China

^d School of Chemistry, University of Nottingham, University Park, Nottingham NG7 2RD, U.K

ARTICLE INFO

Keywords:

CO₂ electroreduction reaction
Electron transfer
Dual-atom catalyst
In situ spectroscopy
Density functional theory

ABSTRACT

Single-atom catalysts (SACs) have emerged as attractive materials for the electrocatalytic carbon dioxide reduction (ECO₂R). Dual-atom catalysts (DACs), an extension of SACs, exhibit more compelling functionalities due to the synergistic effects between adjacent metal atoms. However, the rational design, clear coordination mode, and in-depth understanding of heteronuclear dual-atom synergistic mechanisms remain elusive. Herein, a heteronuclear Ni-Ag dual-atom catalyst loaded on defective nitrogen-rich porous carbon, denoted as Ni-Ag/PC-N, was synthesized using cascade pyrolysis. The configuration of Ni-Ag dual-atom sites is confirmed as N₃-Ni-Ag-N₃. Ni-Ag/PC-N demonstrates a remarkable CO Faradaic efficiency (FE_{CO}) exceeding 90% over a broad range of applied potentials, i.e., from -0.7 to -1.3 V versus reversible hydrogen electrode (RHE). The peak FE_{CO} of 99.2% is observed at -0.8 V (vs. RHE). Tafel analysis reveals that the rate-determining step of ECO₂R-to-CO is the formation of the *COOH intermediate, and Ni-Ag/PC-N exhibits optimal electrokinetics. *In situ* FTIR and *in situ* Raman spectra indicate accelerated production of *COOH intermediates during the ECO₂R-to-CO process. Density functional theory (DFT) calculations demonstrate that the coordinated Ni atom lowers the energy barrier of *COOH intermediates formation over the Ni-Ag/PC-N surface, while the adjacent Ag atom mitigates the catalyst poisoning caused by the strong *CO affinity on the Ni atomic site.

1. Introduction

The excessive utilization of fossil fuels and the resulting emissions of high levels of carbon dioxide (CO₂) have led to significant environmental issues such as energy shortage and global warming [1,2]. To address these global challenges, researchers have turned their attention to electrocatalytic carbon dioxide reduction (ECO₂R) as a promising technology for converting CO₂ using renewable electricity [3]. ECO₂R has the potential to decouple the production of chemical feedstocks from CO₂ emissions, thereby achieving carbon neutrality [4–6]. However, ECO₂R faces several obstacles, including high energy barriers and low selectivity (often measured by Faradaic efficiency, FE). These limitations arise from the chemical inertness and thermodynamic stability exhibited by CO₂ molecules, as evidenced by the substantial bond enthalpy of the C=O double bond, which amounts to 806 kJ mol⁻¹ [7,8]. To overcome

these challenges, there is a pressing need to develop efficient electrocatalysts that exhibit high activity and selectivity in CO₂ conversion. Thus far, researchers have reported various metal-based catalysts with different sizes, such as bulk materials, nanoparticles, sub-nano clusters, and single-atom catalysts (SACs), for the conversion of CO₂ into valuable hydrocarbons [6,9]. However, only a limited number of catalysts have exhibited excellent activity and FEs, along with a clear structure–function relationships.

Transition metals such as Ni, Ag, Co, Fe, when dispersed atomically and anchored on nitrogen-rich porous carbon, have gained significant attention as a novel type of SACs for CO₂ recycling [10–22]. These catalysts are favored for their efficient atomic utilization and the presence of uniform catalytic sites. Among the various Metal-Nitrogen-Carbon (M–N–C) catalysts reported, Ni₁-N_x-C_y sites have demonstrated high FEs towards CO (FE_{CO}) at low applied potentials, e.g., Ni-

* Corresponding authors at: Department of Chemical and Environmental Engineering, and New Materials Institute, University of Nottingham Ningbo China, Ningbo 315100, China.

E-mail addresses: Tao.Wu@nottingham.edu.cn (T. Wu), Mengxia.Xu@nottingham.edu.cn (M. Xu).

<https://doi.org/10.1016/j.cej.2023.146556>

Received 9 August 2023; Received in revised form 26 September 2023; Accepted 7 October 2023

Available online 12 October 2023

1385-8947/© 2023 The Authors. Published by Elsevier B.V. This is an open access article under the CC BY-NC license (<http://creativecommons.org/licenses/by-nc/4.0/>).

NG: 95.0% at -0.73 V vs. reversible hydrogen electrode (RHE) [23] and Ni-N₃-V: 96.1% at -0.66 V vs. RHE [24]. However, the strong binding of *CO on Ni atomic site poses challenges for CO desorption and catalyst poisoning [25,26], leading to a sharp decrease in selectivity at higher applied potentials (over -1.0 V vs. RHE) [27,28]. Meanwhile, previous studies have reported that Ag₁-N_x-C_y can effectively suppress hydrogen evolution reaction (HER) and enhance CO desorption owing to its unique electronic structure [29,30]. However, it has lower-than-desired selectivity and a high energy barrier for *COOH formation during ECO₂R-to-CO, e.g., FE_{CO} of Ag₁-G: 79.2% at -0.70 V vs. RHE [31]; FE_{CO} of Ag-N-C-1: ~70% at -0.85 V vs. RHE [32]. In comparison to SACs, dual-atom catalysts (DACs) show greater potential for improved activity and selectivity in ECO₂R due to the synergistic interactions between adjacent metal atoms [13–17,21,33]. To optimize the performance of DACs in terms of activity and FEs, it is essential to establish the relationship between the catalysts' active site and its ECO₂R-to-CO performance. Accordingly, real-time detection of reaction intermediates and products during ECO₂R plays a crucial role in elucidating this structure–function relationship [34–37]. Traditional characterization techniques are unable to capture the reaction intermediates on the catalyst surface due to the rapid reaction kinetics of ECO₂R and the complexity and low concentration of these intermediates. Therefore, *in situ* spectroscopy and density function theory (DFT) have been employed to monitor the intermediate states in real-time and calculate the energy of adsorbed intermediates [36,38,39].

In this work, we employed a cascade-anchored pyrolysis strategy to precisely synthesize efficient electrocatalyst for ECO₂R-to-CO. The constructed catalyst, denoted as Ni-Ag/PC-N, consists of atomically dispersed Ni-Ag sites embedded in a defective nitrogen-rich porous carbon matrix. To validate the specific coordination model of the catalytic sites on Ni-Ag/PC-N, we conducted X-ray absorption near-edge structure (XANES) and extended X-ray absorption fine structure (EXAFS) spectroscopy. The results indicate that the active site consists of two adjacent Ni and Ag atoms, each is coordinated to three nitrogen atoms and firmly anchored to the defective PC-N matrix, forming the N₃-Ni-Ag-N₃ coordination. Remarkably, Ni-Ag/PC-N exhibits superior ECO₂R performance over a wide potential window (600 mV), reaching a peak FE_{CO} of 99.2% at -0.8 V vs. RHE, with a partial current density of ~ 13 mA cm⁻². To further understand the underlying mechanisms, *in situ* FTIR and *in situ* Raman spectra were used to confirm that the Ni-Ag/PC-N surface effectively stabilizes *COOH intermediates, leading to the production of CO via synergistic effects. Further, DFT calculations provided insights into synergistic effects of the coordinated Ni-Ag pairs. These effects not only lower the energy barrier for *COOH formation on single Ag atoms but also prevent the potential catalyst poisoning effect caused by the high *CO affinity on single Ni atoms. This synergistic facilitation of DACs addresses the common issues associated with SACs and offers promising ways for the precise design and synergetic engineering of atomically dispersed catalysts for ECO₂R.

2. Experimental

2.1. Synthesis of PC carriers

The porous carbon samples were prepared via a typical synthesis procedure [40]. Initially, a total of 800 mg of sodium citrate tribasic hydrate (Na₃C₆H₅O₇·3H₂O, AR) underwent pyrolysis in a porcelain boat. This process was conducted within a tube furnace that operated under an argon atmosphere at a flow rate of 100 sccm. The temperature was gradually increased at a rate of 10 °C per minute, and the pyrolysis occurred at a temperature of 800 °C for a duration of one hour. The resulting black solid was rinsed using dilute H₂SO₄ (0.5 M) to remove the sodium carbonate until no bubbles were observed. The black carbon was then filtered and washed three times with deionized water. Subsequently, the PC sample with a 3-D honeycomb structure was prepared by drying it at 80 °C for a period of 6 h.

2.2. Synthesis of diatomic Ni-Ag/PC-N catalyst

All catalyst samples were prepared using a previously reported synthesis procedure, with a minor modification [40]. In brief, 1.2 g of freshly prepared PC, along with 1.5 mmol of silver nitrate, 67 mmol of α -D-glucose, and 1.5 mmol of nickel nitrate hexahydrate, were mixed with 50 mL deionized water and subjected to ultrasonic treatment for a duration of 2 h. Following this, the resulting solid–liquid mixture was centrifuged twice at 7000 rpm and the remaining solution was slowly decanted off. The moist solids were placed in an oven at 70 °C to dry overnight. The dehydrated mixture was then blended with melamine in a mass ratio of M_{mixture}: M_{melamine} = 1:5. Finally, the mixture was pyrolyzed under an Ar atmosphere at a flowrate of 100 sccm, with a heating rate of 10 °C per min, at a temperature of 800 °C for a duration of 2 h, resulting in the formation of Ni-Ag/PC-N.

2.3. Synthesis of control catalysts

In order to conduct controlled experiments, catalysts of Ni/PC-N and Ag/PC-N were fabricated in the same manner as described above, with the exception of adding only 3.0 mmol of nickel nitrate hexahydrate and 3.0 mmol of silver nitrate, respectively. Additionally, PC-N and Ag-Ni/PC were prepared following a similar procedure, excluding the addition of metal salts and melamine, respectively.

The details of applied chemicals, catalysts characterizations and *in situ* electrochemical spectroscopy measurements involved in this work are provided in the [Supporting Notes](#).

2.4. Preparation of electrode

A total of 10 mg of catalyst, which includes varieties such as Ni-Ag/PC-N, Ni/PC-N, Ag/PC-N, Ni-Ag/PC, PC-N or PC, was dispersed within a mixture containing 50 μ L of Nafion solution (5 wt%) and 1950 μ L of isopropanol, and sonicated for over 1 h. The resulting catalyst slurry, amounting to 100 μ L, was then added dropwise on a pre-cleaned carbon paper measuring 1 \times 1 cm (GDS 180 s, CeTech Co., Ltd) and thoroughly dried in a vacuum oven set at 60 °C.

2.5. Electrochemical performance tests

All electrolysis experiments were conducted within a hermetically-sealed H-type cell (Fig. S1). The cell consists of two compartments, namely the anode chamber and cathode chamber, both with a volume of 50 mL. These compartments were separated by a proton exchange membrane, specifically Nafion-117 from Chemours, which allows only hydrated hydrogen ions to pass through. The electrolysis process employed a three-electrode configuration. In the cathode chamber, the working electrode was a treated carbon paper measuring 1 \times 1 cm, while the reference electrode was an Ag/AgCl electrode saturated with 3 M KCl. Additionally, platinum sheet electrodes measuring 2 \times 2 cm served as the counter electrode in the anode chamber. Both chambers contained a 30 mL aqueous solution of 0.1 M KHCO₃, which was saturated with CO₂ and had a pH of approximately 6.8. To prevent air bubbles from adhering to the electrode surface, a stirrer maintained a speed of 800 rpm in the cathode chamber. An electrochemical workstation, specifically the Gamry Ref. 3000TM, was used to monitor the electrolysis processes and collect electrochemical data. Prior to each electrolysis, a high-purity CO₂ was fed into the chamber at a flow rate of 30 sccm for at least 40 min to ensure a saturated electrolyte. All potential measurements were converted to potentials relative to the reversible hydrogen electrode (RHE) with manual *i*R_u compensation, following the equation below:

$$E \text{ (vs. RHE)} = E \text{ (vs. Ag/AgCl)} + 0.0591 \times \text{pH} + 0.210 - iR_u \times 0.85.$$

Prior to each electrochemical CO₂ reduction, at least five CV scans

were conducted until the curve was smooth to activate the electrocatalyst and eliminate any organic matter present on the electrode surface. The potential range for these scans was set from -0.6 to -2.0 V, reference to Ag/AgCl. Throughout the electrolysis process, high-purity CO_2 (99.999%) was continuously purged into the cathode chamber at a flow rate of 25 sccm. To monitor the resulting gas product (H_2 , CO , CH_4 and C_2H_4), a gas chromatography (GC) inlet was firmly connected to the cathode chamber, enabling real-time detection. The GC system utilized for identification and quantitative analysis of these gas products was the Agilent 8890B, equipped with both a flame ionization detector (FID) and a thermal conductivity detector (TCD). By employing the raw data obtained from GC, the Faradaic efficiencies of the various gas products were determined using Eq. S1.

Linear sweep voltammetry (LSV) measurements were performed in two different solutions: one saturated with CO_2 and the other saturated with Ar, both at a concentration of 0.1 M KHCO_3 . The potential range of the scans was set from 0 to -1.2 V (vs. RHE), with a constant scan rate of 0.1 V s^{-1} . Normally, the electrochemically active specific surface area (ECSA) was found to be directly proportional to the double-layer capacitance (C_{dl}). To determine the C_{dl} , CV scans were initially

performed within the non-Faradaic interval ($E_{\text{open-circuit}} \pm 0.05$ V) at various scan rates (20, 40, 60, 80, 100 and 120 mV s^{-1}). Subsequently, the non-Faradaic currents ($\Delta j = (j_a - j_c)/2$) were plotted at open-circuit potential against the scan rate to obtain the C_{dl} , where j_c and j_a represents the cathodic and anodic current, respectively. Additionally, hydroxide adsorption experiments were performed by conducting oxidative LSV scanning in a 1 M KOH solution saturated with Ar, within a potential range of 0.3 to -0.8 V (vs. RHE) at a scan rate of 5 mV s^{-1} . The Tafel slope was determined by fitting a straight line using the logarithm of the CO partial current density (j_{CO}) as the horizontal coordinate and the overpotential (η) as the vertical coordinate, following Eq. S2.

3. Results and discussion

3.1. Synthesis and characterization of prepared catalysts

The desired Ni-Ag/PC-N materials were synthesized applying a sequential pyrolysis approach with anchoring in a cascade manner [40,41]. Fig. 1a demonstrates the production of porous carbon (PC)

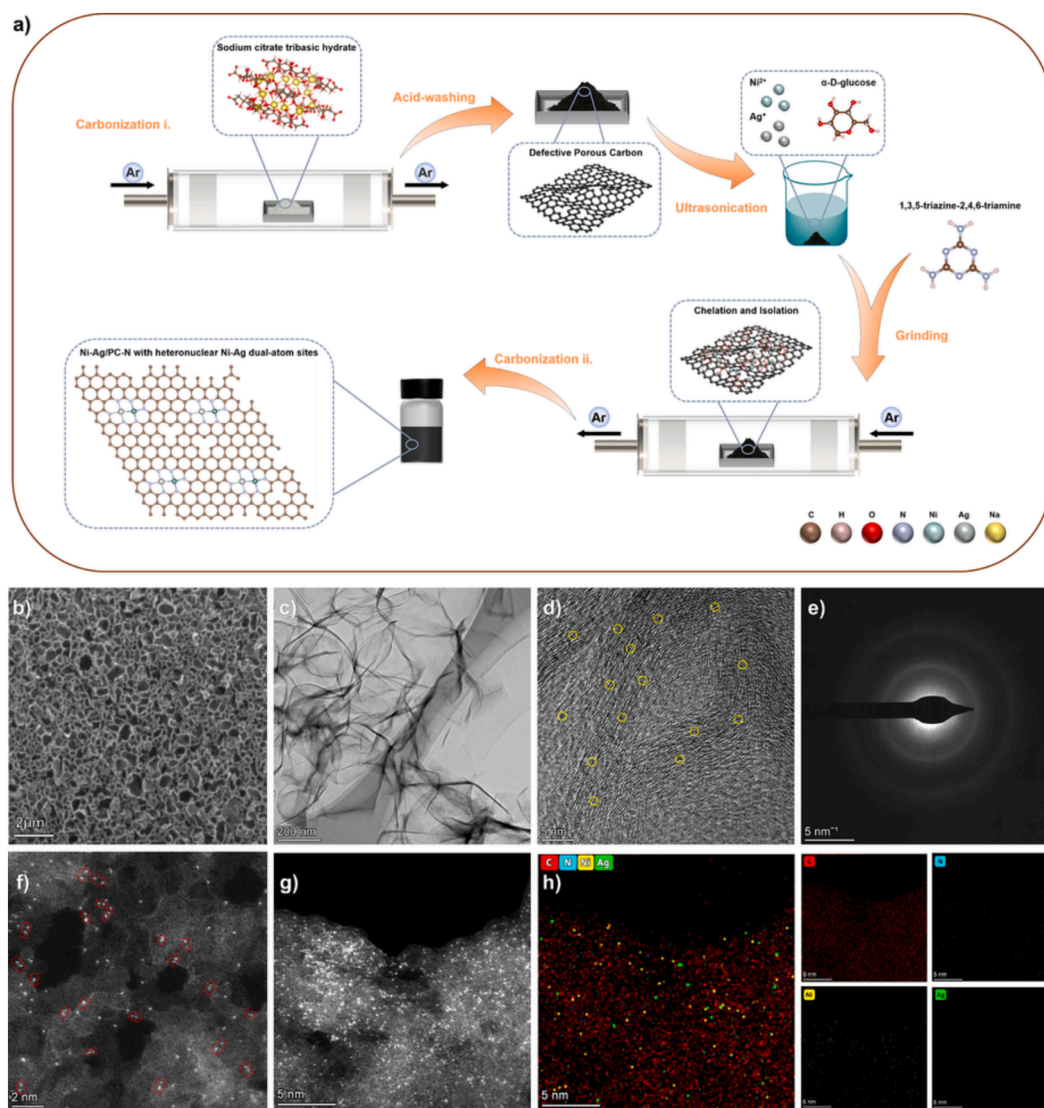


Fig. 1. a) Schematic illustration of the synthesis process of Ni-Ag/PC-N; b) SEM image of PC, c) TEM and d) HRTEM image of Ni-Ag/PC-N. Several lattice distortions are marked with yellow circles; e) SAED pattern of Ni-Ag/PC-N; f) AC-HAADF-STEM images of Ni-Ag/PC-N. Some observed atom pairs are highlighted with red dashed lines; g) AC-HAADF-STEM and h) Corresponding elemental mapping of Ni, Ag, C and N for Ni-Ag/PC-N. (For interpretation of the references to colour in this figure legend, the reader is referred to the web version of this article.)

with a high specific surface area and abundant defects through the pyrolysis of carbon substrates, specifically sodium citrate, which is a more cost-effective alternative to graphene. The PC material was subjected to sulfuric acid washing to eliminate any inorganic impurities, resulting in a 3-D honeycomb-like morphology with ample oxygen-containing groups (Fig. 1b) [40]. Subsequently, the metal salt solution and chelating agent, alpha-D-glucose, were ultrasonically mixed to effectively separate and sequester each metal ion using the domain-limiting effect. It is worth mentioning that the controlled molar ratio of Ni ions to silver ions in the precursor impregnation solution was set at 1:1, aiming to promote the formation of as many Ni-Ag dual-atom pairs as possible to maximize their synergistic effect. The as-prepared PC material was introduced to the mixed solution, allowing the chelated metal ions to be chemically anchored to the PC's oxygen-rich and defect-rich surface. The resulting solid-liquid mixture underwent sequential ultrasonic dispersion, high-speed centrifugation, and decanting, followed by thorough drying in a vacuum. Prior to the second pyrolysis step, the PC material, anchored with metal complexes, was physically ground and thoroughly mixed with the nitrogen source material, melamine. During pyrolysis, the chelated metal complexes decomposed at approximately 500 °C, forming residues that prevented the aggregation of metal atoms. Furthermore, these protected metal atoms combined with the carbon-nitrogen species (PC-N) from melamine decomposition at around 800 °C, resulting in the formation of the M-N-C coordination.

Based on the powder X-ray diffraction (PXRD) pattern (Fig. S2), it can be observed that the PC, Ni/PC-N, and Ni-Ag/PC-N samples all exhibit only two broad peaks at approximately 24.1° and 44.1°, indicating the presence of graphitic carbon and absence of any crystalline impurities or metal particles. However, in the PXRD pattern of Ag/PC-N, characteristic diffraction peaks of Ag are observed. The excessive concentration of Ag precursor solution results in the formation of Ag clusters under the same synthesis conditions. This phenomenon is evident in the tendency of free Ag atoms generated during pyrolysis to diffuse and aggregate into clusters on the PC-N surface. Conversely, when the concentration of AgNO₃ was reduced and Ni atoms were introduced to achieve their coexistence and distribution on PC-N, the diffusion of Ag atoms is restricted, and they are stabilized by the nearby Ni atoms [14,32]. The PC-N and Ni-Ag/PC-N samples show a three-dimensional honeycomb-like porous structure, as observed in the scanning electron microscopy (SEM) and transmission electron microscopy (TEM) images (Fig. 1b, S3–S6). This porous structure facilitates mass transfer during ECO₂R [26].

Furthermore, the lamellar morphology of the dispersed Ni-Ag/PC-N, which is characteristic of pyrolyzed carbonaceous materials and favors single-atom loading, is evident in the high-resolution transmission TEM (HRTEM) images (Fig. 1c and S6). Notably, the HRTEM image (Fig. 1d) reveals distinct lattice-distortion defects in the carbon substrate, marked by yellow circles, possibly attributed to the coordination of dispersed Ni/Ag hetero-diatom pairs with N atoms during the stepwise carbonization process. Additionally, Fig. 1e presents a selected area electron diffraction (SAED) image of the Ni-Ag/PC-N sample, displaying a ring pattern indicative of amorphous carbon, consistent with the PXRD pattern. For a closer examination of the distribution of metal single-atoms, aberration-corrected high-angle annular dark field scanning transmission electron microscopy (AC-HAADF-STEM) images confirm the uniform dispersion of Ni and Ag sites, measuring approximately 0.15 nm in size, in the Ni-Ag/PC-N sample (Fig. S7).

Interestingly, the presence of neighboring dual-dot sites is observed and circled by the red dashed line, providing indications of the existence of diatomic sites (Fig. 1f and S7). Energy dispersive X-ray spectroscopy (EDS) analysis further confirms the uniform distribution of Ni, Ag and N elements on the carbon matrix without any aggregation (Fig. 1g, h and S7). Besides, inductively coupled plasma mass spectrometry (ICP-MS) results demonstrate that the mass percentages of Ni and Ag in Ni-Ag/PC-N are 0.46% and 6.60% (7.06% in total), respectively, which are higher than those of Ni/PC-N (0.69%) and Ag/PC-N (2.96%) (Table S1). This

higher metal loading capacity of Ni-Ag/PC-N can be attributed to the interaction between Ni and Ag species, which stabilize each other and form coordinated heteronuclear dual-metal sites [20,42]. Additionally, the intensity ratio of the D-band to G-band (I_D/I_G) obtained from Raman spectroscopy serves as an indicator for structural imperfections in carbon materials. The Raman spectra display two prominent peaks at around 1338 and 1589 cm⁻¹, corresponding to the in-plane stretching vibration of C-atoms sp² hybridization and defects within the C-atom lattice, respectively [28,32,43].

Fig. 2a indicates that the concentration of inner defects in PC, PC-N and Ni-Ag/PC-N significantly increases during cascade pyrolysis processes ($I_D/I_G = 0.97, 1.01$ and 1.08 , respectively). This indicates that the abundance of defects in the carbon matrix facilitates the reaction kinetics during electrocatalytic reactions [44]. Furthermore, the Ni-Ag/PC-N sample possesses a high Bruno-Emmett-Teller (BET) specific surface area of 303 m² g⁻¹ compared to the other samples (Table S2) due to its porous and defective structure formed during the stepwise carbonization process [32]. The N₂ adsorption isotherms confirm the presence of layered mesopores and micropores in the sample, which greatly enhances mass transfer during the ECO₂R process (Fig. 2b) [45].

Additionally, the CO₂ adsorption isotherms demonstrate that the Ni-Ag/PC-N catalyst has a higher CO₂ adsorption capacity of 1.02 mmol g⁻¹ compared to PC (0.60 mmol g⁻¹) and PC-N (0.55 mmol g⁻¹), indicating more CO₂ molecules can be adsorbed on its surface (Fig. 2c) [32]. Electron paramagnetic resonance (EPR) spectroscopy is commonly utilized to characterize the defect properties of M-N-C materials. All four samples exhibit similar characteristic peaks in their EPR spectra, with a g factor of 2.002. These peaks are associated with unpaired electrons on the conjugated CN aromatic ring [46]. The source of these unpaired electrons can be attributed to C-vacancies, with the highest concentration of C-vacancies observed in the Ni-Ag/PC-N samples (Fig. 2d). The presence of an abundance of unpaired electrons from C-vacancies at the interface enhances the electronic properties of Ni-Ag/PC-N and creates potential catalytic sites for ECO₂R, thereby leading to its exceptional catalytic performance [47].

3.2. Atomic structure of Ni-Ag/PC-N catalysts

X-ray photoelectron spectroscopy (XPS), X-ray absorption near edge structure (XANES) and extended X-ray absorption fine structure (EXAFS) spectroscopy techniques provide valuable insights into the valence information and coordination environment of the metal centers in Ni-Ag/PC-N. The N 1s spectrum obtained from the high-resolution XPS analysis of Ni-Ag/PC-N (Fig. 2e) reveals five distinct peaks representing different nitrogen species: pyridinic-N (398.3 eV), metal-N (399.6 eV), pyrrolic-N (400.0 eV), graphitic-N (400.9 eV) and oxidized-N (401.7 eV) [14,15,17]. Notably, the as-prepared materials show porphyrin-like moieties at 399.6 eV, which are assigned to metal-nitrogen (M-N) coordination. Moreover, the area proportion of characteristic M-N peaks (399.6 eV) increases with the higher mass percentage of the metal element in the catalyst (Fig. 2e, Table S1) [21], suggesting the coexistence and stabilization of Ag and Ni species are primarily coordinated to nitrogen rather than forming nanoparticles or clusters [20]. This observation, combined with the high density of atomic pairs observed (Fig. 1f), supports the postulation of the formation of Ni/Ag dual-metal sites in the Ni-Ag/PC-N sample. Further analysis of the XPS curves of Ni 2p and Ag 3d reveals that the Ni 2p_{3/2} peak in the Ni-Ag/PC-N sample appears at around 854.90 eV, between the Ni⁰ 2p_{3/2} (~852.9 eV) and Ni²⁺ 2p_{3/2} (~856.0 eV) peaks. Similarly, the Ni 2p_{1/2} peak (~872.48 eV) falls within the interval of Ni⁰ 2p_{1/2} (~870.5 eV) and Ni²⁺ 2p_{1/2} (~873.5 eV) (Fig. S8a) [7,28,34]. The Ag 3d XPS spectrum exhibits two peaks at approximately 374.08 eV and 368.2 eV, corresponding to Ag 3p_{3/2} and Ag 3p_{5/2}, respectively. These peaks have higher binding energies compared to Ag⁰ 3d_{3/2} (~373.4 eV) and Ag⁰ 3d_{5/2} (~368.0 eV) and are close to Ag⁺¹ 3d_{3/2} (~374.3 eV) and Ag⁺¹ 3d_{5/2} (~368.3 eV) (Fig. S8b) [30,31]. In summary, the chemical state

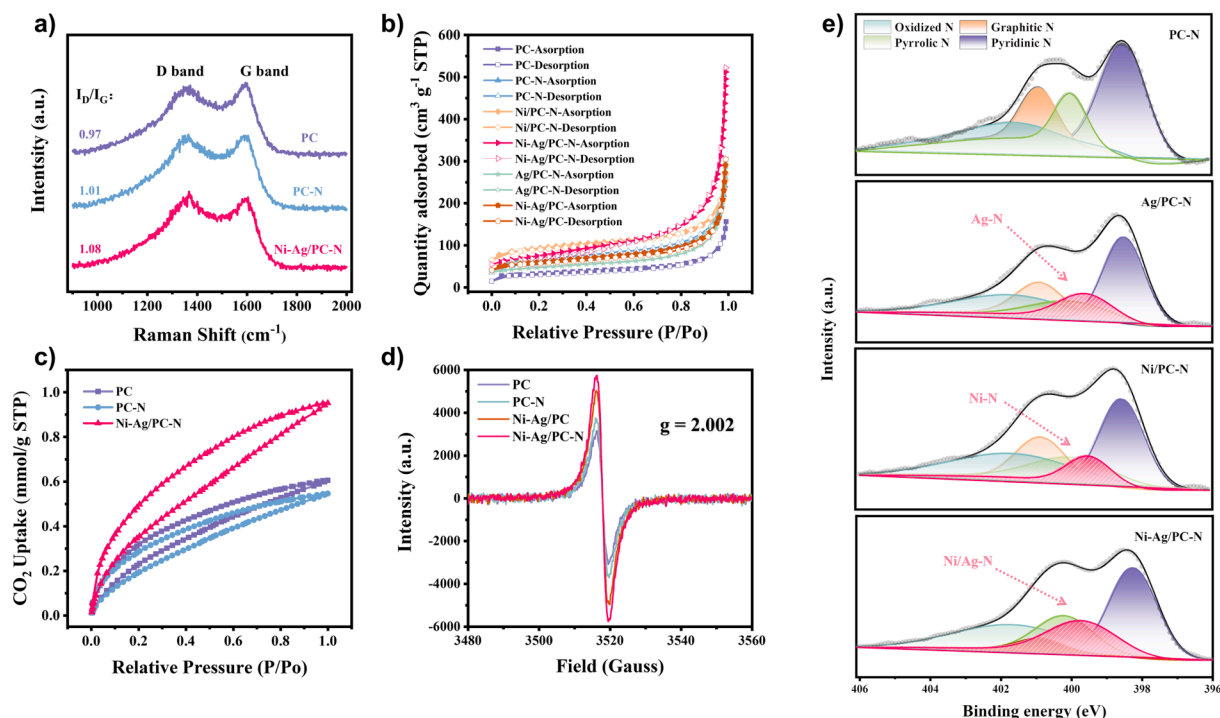


Fig. 2. a) Raman spectra of PC, PC-N and Ni-Ag/PC-N; b) N_2 adsorption–desorption isotherms of PC, PC-N, Ni/PC-N, Ni-Ag/PC-N, Ag/PC-N and Ni-Ag/PC; c) CO_2 adsorption measurements of PC, PC-N and Ni-Ag/PC-N; d) EPR spectra of C-vacancies in PC, PC-N, Ni-Ag/PC and Ni-Ag/PC-N; e) High-resolution XPS N 1s spectrum of PC-N, Ag/PC-N, Ni/PC-N and Ni-Ag/PC-N.

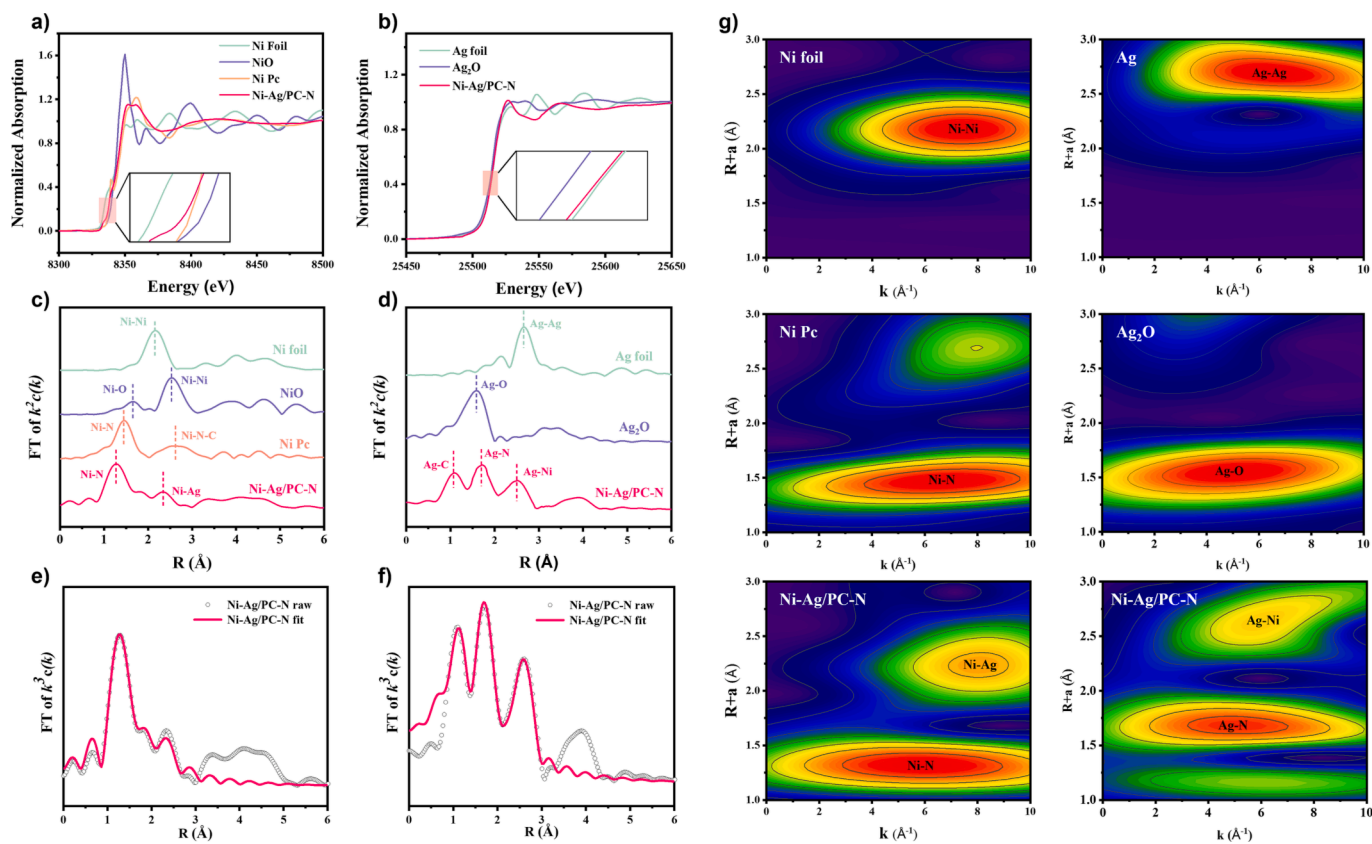


Fig. 3. a) Ni K-edge XANES spectra of Ni foil, NiO, Ni PC, and Ni-Ag/PC-N; b) Ag K-edge XANES profiles of Ag foil, Ag_2O , and Ni-Ag/PC-N. Fourier transformation of c) Ni K-edge XANES and d) Ag K-edge XANES spectra at R space. The corresponding Ni K-edge e) and Ag K-edge f) EXAFS fitting curves for Ni-Ag/PC-N at R space, respectively; g) WT k^3 -weighted EXAFS contour plots of Ni K-edge for Ni foil, Ni PC, Ni-Ag/PC-N and Ag K-edge for Ag foil, Ag_2O , and Ni-Ag/PC-N.

of Ni 2p in the Ni-Ag/PC-N sample lies between 0 and + 1, while Ag 3d exhibits a chemical state above 0 and close to + 1, which aligns with the commonly estimated valence state of SACs (Figs. S8–S10).

In order to gain a comprehensive understanding of the coordination modes and chemical states of the Ni and Ag centers in Ni-Ag/PC-N, additional XANES and EXAFS measurements were conducted. The Ni K-edge XANES results (Fig. 3a) show that the adsorption threshold of the Ni-Ag/PC-N sample lies between that of the Ni foil and the NiO standard samples. This observation provides valence information for $\text{Ni}^{\delta+}$ ($0 < \delta < 2$) in the Ni-Ag/PC-N samples, which aligns with the previously obtained XPS results [26,28]. Additionally, the inset of Fig. 3a highlights the leading edge feature at approximately 8336 eV, indicating the hybridization of the 3p and 4p orbital of the Ni central atom [7]. The higher peak intensity in Ni-Ag/PC-N, resulting from the distorted D_{4h} symmetry, is comparable to the nickel phthalocyanine (Ni-Pc) standard sample [7]. These observations suggest that the Ni center in Ni-Ag/PC-N exhibits a typical metal-nitrogen ($M-N_x$) coordination similar to that of the Ni-Pc standard, but with the distortion of the D_{4h} symmetry attributed to another metal-metal (M_1-M_2) coordination [42]. Furthermore, the Ag K-edge XANES results on the same samples demonstrate that the intensity of the Ni-Ag/PC-N samples is greater than that of the Ag foil and slightly less intense than the Ag_2O standard samples (Fig. 3b). This indicates that the valence information of $\text{Ag}^{\gamma+}$ ($0 < \gamma < 1$) in the Ni-Ag/PC-N is consistent with the results obtained from the XPS analysis.

The comparison between Ag foil and Ni-Ag/PC-N reveals that the absorption edge position of Ni-Ag/PC-N is skewed towards the higher energy side. This indicates that the Ag species are positively charged and firmly attached to the surface of the PC-N carrier as electron donors, thus forming $M-N_x$ sites [32]. The Fourier transform (FT) k^2 weighted EXAFS spectra were further employed to provide more detailed information about the $M-N_x$ and M_1-M_2 coordination mentioned earlier. Through comparison with other standard samples (Fig. 3c), it is observed that the peaks at 1.30 Å and 2.33 Å in the k^2 -weight FT spectra from Ni K-edge EXAFS can be attributed to $M-N_x$ and M_1-M_2 coordination, respectively. Notably, the characteristic peak at 1.30 Å may be ascribed to Ni-N, as evidenced by the comparison with the FT curve of the Ni Pc sample. Interestingly, the M_1-M_2 peak observed for Ni-Ag/PC-N at 2.33 Å is not found in the Ni foil and NiO standard samples, providing further evidence for the presence of Ni-Ag coordination. Similarly, the k^3 -weight FT spectra from Ag K-edge EXAFS of the same Ni-Ag/PC-N samples exhibit peaks at 1.10 Å, 1.68 Å and 2.57 Å, which can be assigned to Ag-C, Ag-N and Ag-M coordination, respectively (Fig. 3d). In contrast to the Ag foil reference spectrum, the peak at 2.70 Å for the Ag-Ag coordination is not detected in Ni-Ag/PC-N, thereby confirming that the coordination mode of M_1-M_2 as an Ag-Ni coordination.

To support the arrangement of Ni-Ag dual-atom sites on PC-N, wavelet transforms (WTs) were performed using high-resolution in R -space and k -space (Fig. 3e and f). The WT-EXAFS contour plots of the Ni-Ag/PC-N sample, both at the Ni K-edge and Ag K-edge, show peak intensities at approximately 4.3 \AA^{-1} , which corresponds to the Ni-N and Ag-N coordination [17,31]. Furthermore, a sub-maximal intensity at around 6.2 \AA^{-1} indicates the presence of heteronuclear dual-atom Ni-Ag coordination in Ni-Ag/PC-N, which is noticeably different from the Ni-Ni coordination (7.6 \AA^{-1}) and Ag-Ag (7.2 \AA^{-1}) coordination in Ni foil and Ag standard samples (Fig. 3g and S11) [7,32]. By fitting the results to Ni K-edge EXAFS and Ag K-edge EXAFS, quantitative coordination information regarding Ni and Ag atoms in Ni-Ag/PC-N is obtained. The analysis of Ni K-edge EXAFS reveals a coordination number of 3.1 for Ni-N bonding and a coordination number of 1.0 for Ni-Ag bonding (Fig. 3e and Table S3). Similarly, the fitting results of Ag K-edge EXAFS confirms an Ag-N coordination number of 3.3 and an Ag-Ni coordination number of 1.5 (Fig. 3f and Table S4). In summary, the local coordination conformation of the heteronuclear Ni/Ag dual-atom site in Ni-Ag/PC-N is quantitatively determined as $\text{N}_3\text{-Ni-Ag-N}_3$ coordination. Both the Ni foil and Ag standard samples exhibit a coordination number

of 12, indicating the atomic dispersion of Ni and Ag species in the Ni-Ag/PC-N samples. This observation aligns with the previously discussed characterization findings, including XRD, HADDF-STEM, XPS, and other relevant analyses.

3.3. Electrocatalytic performance of catalysts

The electrocatalytic performance of the catalysts (Ni-Ag/PC-N, Ni-Ag/PC, Ni/PC-N, Ag/PC-N, PC-N, PC) was initially evaluated by linear sweep voltammetry (LSV) in a conventional gastight H-cell reactor in a CO_2 - and Ar-saturated 0.1 M KHCO_3 solution. The current density in this study was standardized to the electrode's geometric surface area. Among the synthesized catalysts, Ni-Ag/PC-N exhibits the lowest applied potential of -0.72 V to achieve a current density of 10 mA cm^{-2} in a CO_2 -saturated electrolyte. In comparison, the applied potentials required to maintain the same current density for Ni/PC-N, Ni-Ag/PC, Ag/PC-N, PC-N, and PC are -0.82 , -0.98 , -1.06 , -1.07 , and -1.08 V , respectively (Fig. 4a). Notably, when comparing the LSV curves of Ni-Ag/PC-N in Ar- and CO_2 -saturated electrolytes, a significant increase in current density and onset potential are observed (Fig. 4a). This suggests that the Ni-Ag/PC-N catalyst demonstrates sensitivity to the presence of CO_2 molecules in the electrolyte and exhibits effective electrocatalysis for CO_2 reduction rather than HER [20]. To gain a more comprehensive understanding of the ECO_2R activity and the product distribution across six as-prepared catalysts, potentiostatic CO_2 electrolysis was conducted at potentials ranging from -0.7 V to -1.3 V (vs. RHE) for 2 h at 0.1 V intervals. The gas and liquid products were detected by online gas chromatography (GC) and offline nuclear magnetic resonance (NMR) spectroscopy. The calibration curves for the various gas products and the original chromatograms are included in the Supporting Information (Figs. S12 and S13). The results reveal that the quantified gas products, CO and H_2 , exhibit a total Faradaic efficiency close to 100%.

The results depicted in Fig. 4b and S14 exhibit that Ni-Ag/PC-N maintains a high FE_{CO} above 90% within the potential range of -0.7 V to -1.3 V (vs. RHE). Notably, at a potential of -0.7 V , Ni-Ag/PC-N achieved a FE_{CO} of 94.8%. As the potential becomes more negative, Ni-Ag/PC-N reaches its peak FE_{CO} of 99.2% at -0.8 V . However, at an applied potential of -1.3 V , its FE_{CO} decreases slightly to 93.1%. This decrease can be attributed to the limitation of CO_2 dissolution in the 0.1 M KHCO_3 solution, which hinders mass transfer, and the increased participation of electrons in HER [36]. Fig. 4c demonstrates the dependence of the partial current density (j_{CO}) on the operating potential. At -0.8 V , the j_{CO} of the Ni-Ag/PC-N sample is 12.6 mA cm^{-2} , which is considerable higher than the j_{CO} values of Ni/PC-N (7.3 mA cm^{-2}), Ag/PC-N (4.2 mA cm^{-2}), Ni-Ag/PC (3.2 mA cm^{-2}), PC (2.0 mA cm^{-2}) and PC-N (1.7 mA cm^{-2}), with enhancement factors of 1.7, 3.0, 3.9, 6.3, and 7.4, respectively. This clearly demonstrates the superior performance of Ni-Ag/PC-N in terms of j_{CO} compared to other catalysts. This remarkable and continuous improvement in the j_{CO} of Ni-Ag/PC-N over Ni/PC-N and Ag/PC-N can be attributed to its excellent conductivity and high electron selectivity, resulting from the synergistic interactions in the heteronuclear Ni-Ag coordination configuration. These factors optimize electron transport and facilitates ECO_2R -to-CO [14]. Overall, the synthesized Ni-Ag/PC-N exhibits superior ECO_2R -to-CO performance compared to other reported high-performance dual-atom catalysts for ECO_2R -to-CO in H-cell, as shown in Fig. 4h and Table S5 [26,28–32,49–51]. Moreover, Ni-Ag/PC-N also exhibits good stability under 10 h amperometric i -t tests (at -0.8 V vs. RHE, see Fig. S15).

To unravel the underlying factors contributing to the exceptional catalytic activity of the Ni-Ag/PC-N catalyst, a comprehensive electrokinetic study was performed to elucidate the mechanism of CO_2 reduction on the heteronuclear Ni-Ag dual-atom sites. Building upon the previously reported electrochemical mechanism of CO_2 reduction to CO, four fundamental reaction steps can be proposed as shown in the following equations (* denotes the active site): [34].

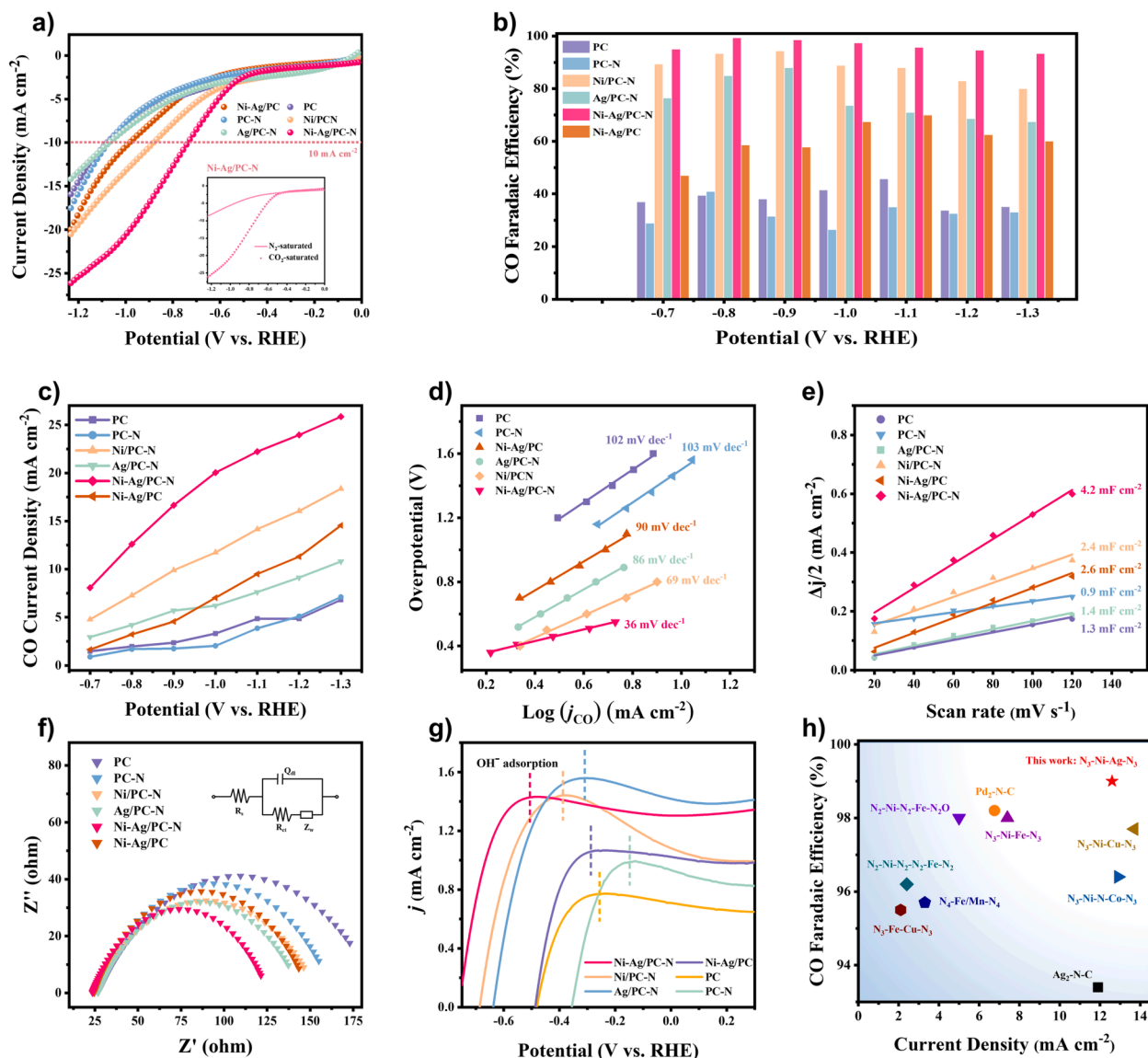
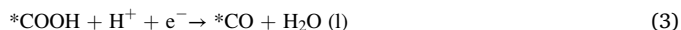


Fig. 4. Electrochemical performances of ECO₂R over PC, PC-N, Ni/PC-N, Ag/PC-N, Ni-Ag/PC, and Ni-Ag/PC-N. a) LSV curves in CO₂-saturated 0.1 M KHCO₃ solution. The inset figure is LSV curves of Ni-Ag/PC-N in Ar-saturated 0.1 M KHCO₃ solution; b) CO Faradaic efficiency of ECO₂R from -0.7 V to -1.3 V vs. RHE, c) CO partial current density, d) Tafel curves for the CO partial current density, e) ECSA curves and f) EIS curves of as-prepared catalysts; g) Single oxidative LSV scans in Ar-saturated 0.1 M KOH of different catalysts; h) FE_{CO} value of Ni-Ag/PC-N in this work and other reported high-performance dual-atom catalysts for ECO₂R-to-CO [14–17,19–21,33,48].



The rate-determining step (RDS) in the ECO₂R-to-CO process is heavily influenced by the electrode material's characteristics, such as the type of metal center and the coordination environment of the active sites. To determine the RDS of Ni-Ag/PC-N in the ECO₂R process, the corresponding Tafel slopes of the catalysts were fitted and analyzed. Remarkably, the Tafel slope of Ni-Ag/PC-N is found to be 36 mV dec⁻¹, which is lower than that of Ni/PC-N (69 mV dec⁻¹), Ag/PC-N (86 mV dec⁻¹), Ni-Ag/PC-N (90 mV dec⁻¹), and PC (102 mV dec⁻¹), while the maximum value observed for PC-N is 103 mV dec⁻¹ (Fig. 4d). This small Tafel slope of Ni-Ag/PC-N indicates its remarkable kinetic properties in

the ECO₂R-to-CO process. Furthermore, the theoretically calculated Tafel slopes for ECO₂R are 118 mV dec⁻¹ (for the single electron transfer step, ET) and 59 mV dec⁻¹ (for the single proton transfer step, PT), respectively. Notably, the experimentally observed Tafel slope of Ni-Ag/PC-N closely aligns with the theoretical slope of 59 mV dec⁻¹. This suggests that the initial ET step (Eq. 1) does not serve as the RDS for this reaction, while the subsequent PT step (Eq. 2) is a more plausible candidate for the RDS of the Ni-Ag/PC-N catalyst [20,52]. These aforementioned findings will be further corroborated and elucidated by *in situ* spectroscopy techniques (*in situ* FTIR and *in situ* Raman) as well as DFT calculations.

To gain insights into the underlying factors contributing to the exceptional electrocatalytic performance, the electrochemically active surface area (ECSA) of the cathode catalyst was evaluated by quantifying the electrochemical double-layer capacitance (C_{dl}) (Fig. 4e and S16). The C_{dl} values obtained follow the order of PC-N (0.9 mF cm⁻²) < PC (1.3 mF cm⁻²) < Ag/PC-N (1.4 mF cm⁻²) < Ni/PC-N (2.4 mF cm⁻²) < Ni-Ag/PC (2.6 mF cm⁻²) < Ni-Ag/PC-N (4.2 mF cm⁻²), which can be

attributed to the higher metal density and active heteronuclear Ni/Ag coordination in Ni-Ag/PC-N. These findings further support the electrokinetic properties of Ni-Ag/PC-N that favor the ECO_2R -to-CO process, which is consistent with the observations from the Tafel analysis. Electrochemical impedance spectroscopy (EIS) was also conducted to examine the kinetic advantages of Ni-Ag/PC-N by analyzing the catalyst's charge transfer resistance (R_{ct}) obtained from semicircles in the low-frequency region. The R_{ct} value of Ni-Ag/PC-N is found to be 101.9 Ω , which is lower than that of Ag/PC-N (118.1 Ω), Ag-Ni/PC (125.0 Ω), Ni/PC-N (129.7 Ω), PC-N (138.7 Ω), and PC (162.7 Ω) (Fig. 4f and Table S6). Among these catalysts, Ni-Ag/PC-N exhibits the lowest R_{ct} value, indicating more efficient charge transfer and reaction kinetics, leading to a faster ECO_2R -to-CO process (Eqs. 1–4). Additionally, the adsorption affinity of the intermediate $^*\text{CO}^{2-}$ on the electrode surface was investigated by using OH^- species as a surrogate for $^*\text{CO}^{2-}$ in the experiments [53,54]. The adsorption of OH^- was carried out through oxidized LSV low-rate scan under N_2 -saturated 0.1 M KOH electrolyte. The OH^- adsorption potentials follow the order of Ni-Ag/PC-N (−0.50 V) < Ni/PC-N (−0.38 V) < Ag/PC-N (−0.31 V) < Ag-Ni/PC (−0.28 V) < PC (−0.25 V) < PC-N (−0.14 V) (Fig. 4g). The Ni-Ag/PC-N catalyst, with its abundant defects and special heteronuclear Ni-Ag coordination conformation, exhibits a more negative potential for OH^- adsorption, indicating the highest binding affinity for the intermediate $^*\text{CO}^{2-}$ and promoting the formation of $^*\text{COOH}$.

3.4. In situ spectral observations of ECO_2R over Ni-Ag/PC-N surface

In order to further validate the conclusions drawn from the Tafel

slope and OH^- adsorption analysis, a time-dependent *in situ* FTIR spectrum was acquired to examine the details of the reaction intermediates over the heteronuclear Ni-Ag dual-atom sites. Following a potentiostatic electrolysis at −1.0 V for a duration of 20 min, a gradual emergence of absorption peaks ranging from 1200 to 2000 cm^{-1} is observed (Fig. 5a and S17). The IR bands at approximately 1400 and 1740 cm^{-1} , corresponding to symmetrical and asymmetrical stretching vibrations in carbonate groups (HCO_3^-), are attributed to the dissolution of CO_2 in water [34]. It is important to note that a significant IR peak at 1547 cm^{-1} is also identified, and its intensity increases remarkably over time. This absorption peak is believed to represent the carboxyl group of COOH^* (Fig. 5b), which serves as a crucial intermediate in the ECO_2R -to-CO (PT step, Eq. 2) [35,55,56]. This finding demonstrates that the Ni-Ag dual-atom sites effectively facilitate the activation of $^*\text{CO}_2$ to form the intermediate product COOH^* and enhance the rate of RDS for ECO_2R .

In order to support the findings, potential dependent *in situ* surface-enhanced Raman spectra were applied to investigate the active sites and adsorbed intermediates on the Ni-Ag/PC-N catalyst. The applied potential was systematically decreased in increments of 100 mV from −0.05 to −1.85 V during the *in situ* Raman spectroscopy test, and data were also recorded under open circuit potential (OCP) conditions. As depicted in Fig. 5c, a Raman peak at approximately 249 cm^{-1} is observed in the low wavenumber region, which could be assigned to the Ni/Ag-N stretching vibration peak [57]. Moreover, Raman bands at 648 cm^{-1} and 1060 cm^{-1} are observed, originating from the vibrational modes of CO_3^{2-} ($\nu_1\text{CO}_3^{2-}$) in the electrolyte solutions. Although HCO_3^- is the dominant carbonaceous species in the applied electrolyte, the

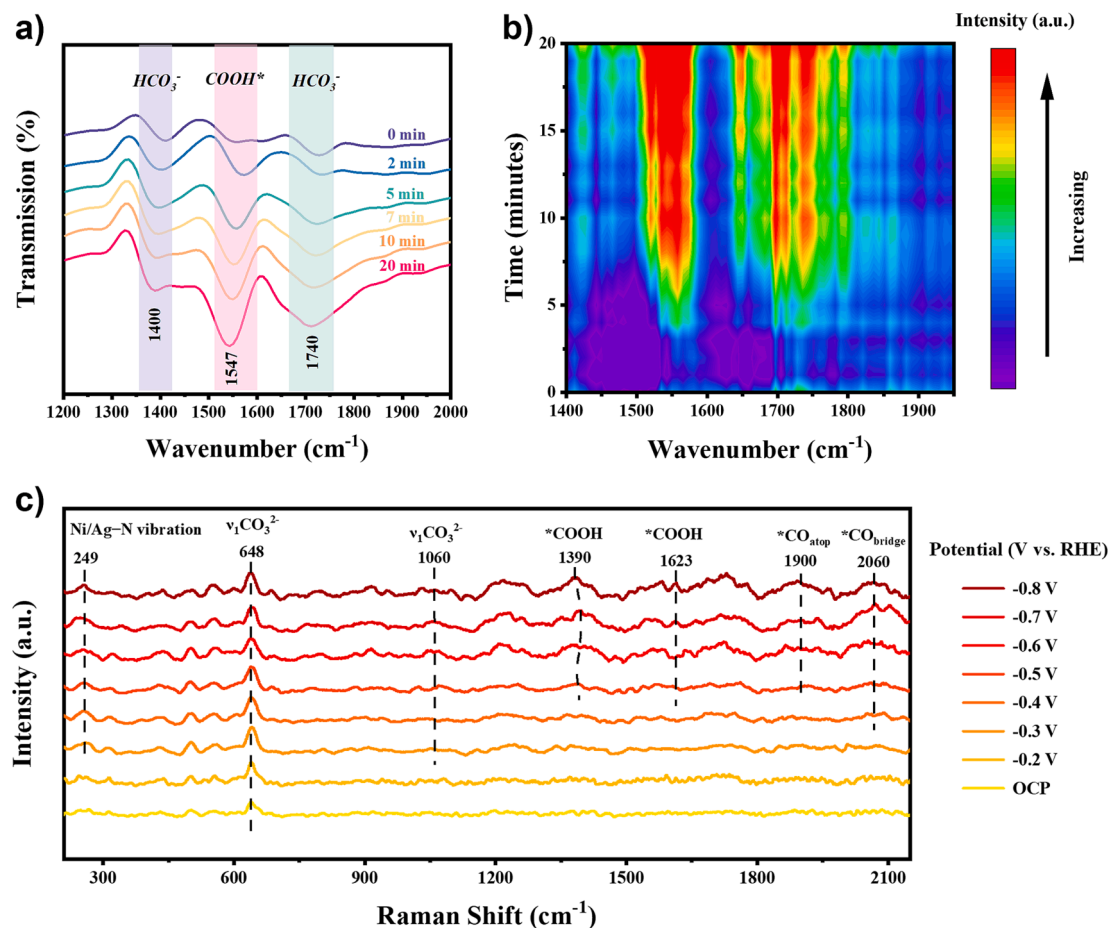


Fig. 5. a) Time-dependent electrochemical *in situ* FTIR spectra of the Ni-Ag/PC-N at the potential of −0.8 V vs. RHE. All spectroscopic tests were conducted in CO_2 -saturated 0.1 M KHCO_3 ; b) Corresponding 2D contour colour fill to the line plots; c) Potential-dependent *in situ* Raman spectra of the Ni-Ag/PC-N recorded after cyclic voltammetry (CV) scan at OCP and the applied potential ranges from −0.2 to −1.2 V vs. RHE with the potential interval of 0.1 V for 10 min.

presence of CO_3^{2-} as an adsorbed species could be explained by the phenomena of physisorption and chemisorption [39]. Apart from the $\nu_1\text{CO}_3^{2-}$ peak, Raman bands at 1900 cm^{-1} and 2060 cm^{-1} are observed, which could be attributed separately to the νCO of $^*\text{CO}$ on atop/bridge sites [38]. Notably, the Raman characteristic peaks at 1380 cm^{-1} and 1623 cm^{-1} are identified as the C-O stretching and C=O stretching of the reaction intermediate $^*\text{COOH}$, respectively [37,39]. This *in situ* Raman analyses further confirm the preferential nature of Ni-Ag/PC-N with heteronuclear dual-atom sites for the proton transfer step in the ECO_2R -to-CO process.

3.5. Theoretical study of heteronuclear Ni-Ag dual-atom for ECO_2R

To theoretically unveil the underlying factors contributing to the enhanced activity of neighboring Ni-Ag sites in ECO_2R , DFT calculations were conducted based on the EXAFS fitting results. Specifically, the adsorption energy of intermediates on Ni ($\text{N}_3\text{-Ni}^*\text{-Ag-N}_3$), Ag ($\text{N}_3\text{-Ni-Ag}^*\text{-N}_3$) and Ni-Ag ($\text{N}_3\text{-Ni}^*\text{-Ag}^*\text{-N}_3$) coordination modes were simulated, using the $\text{N}_3\text{-Ni-Ag-N}_3$ coordination as a basis. The optimal model with the lowest free energy is determined to be $\text{N}_3\text{-Ni}^*\text{-Ag-N}_3$, as shown in Fig. 6a. Additionally, the charge density differences of key

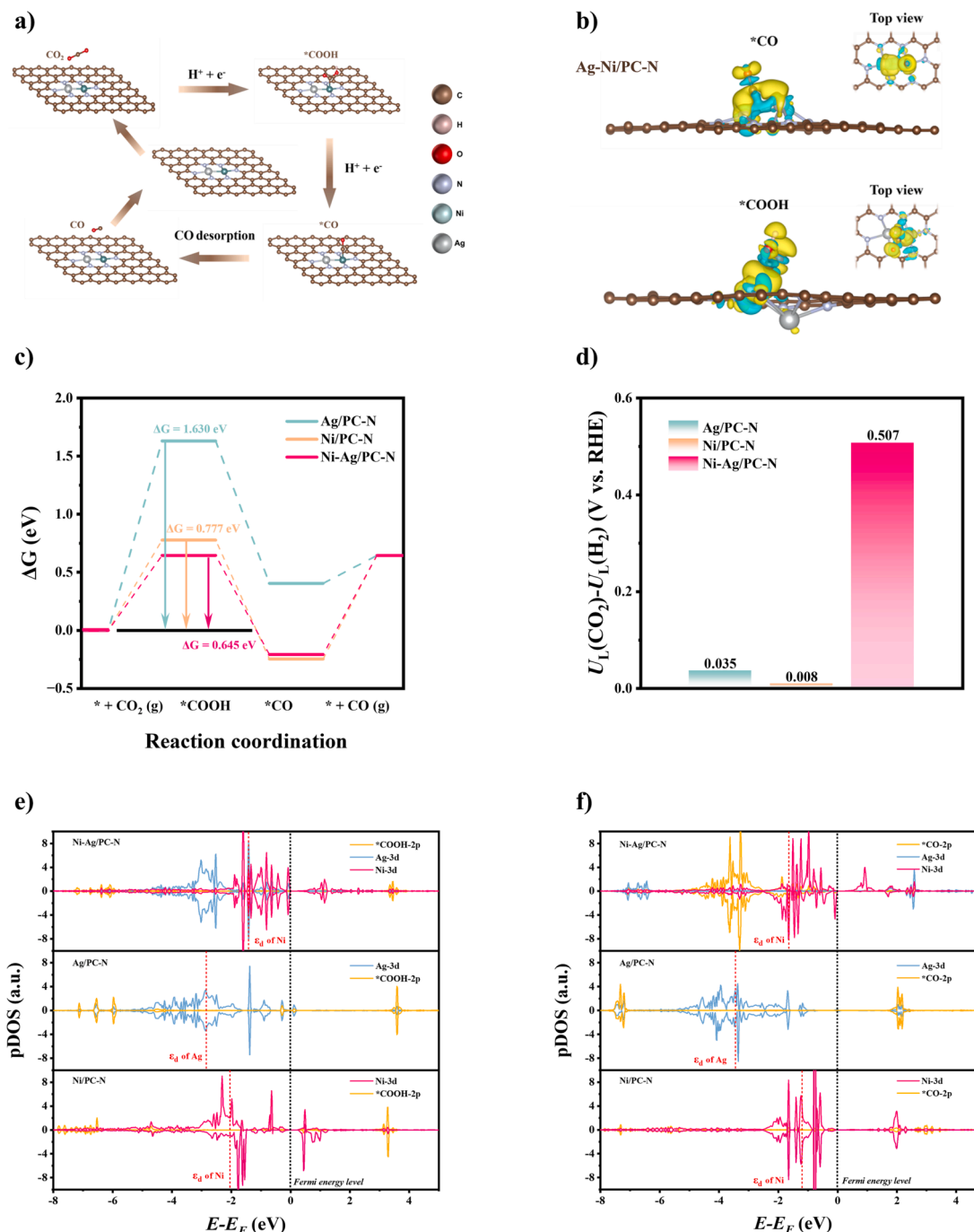


Fig. 6. a) Schematic of the ECO_2R -to-CO mechanism of $\text{N}_3\text{-Ni}^*\text{-Ag-N}_3$; b) Charge density difference of intermediates $^*\text{CO}$ and $^*\text{COOH}$ on the Ni-Ag/PC-N, Ag/PC-N and Ni/PC-N site, isosurface value is set to be $0.002\text{ e}/\text{\AA}^3$, the yellow and cyan indicate the electron accumulation and electron depletion, respectively; c) Gibbs free energy diagram of ECO_2R -to-CO process, and d) Differences in theoretical limiting potential for ECO_2R and HER of Ag/PC-N, Ni/PC-N and Ni-Ag/PC-N; e&f) Projected densities of states for Ni/Ag-3d and C-2p orbitals of Ni-Ag/PC-N, Ni/PC-N and Ag/PC-N adsorbed different $^*\text{CO}/^*\text{COOH}$ intermediates. (For interpretation of the references to colour in this figure legend, the reader is referred to the web version of this article.)

intermediates (*COOH and *CO) over Ni-Ag/PC-N, Ni/PC-N and Ag/PC-N were calculated, as depicted in Fig. 6b and S18. The results provide compelling evidence of significant electron interactions occurring among the dual-atom Ni-Ag pair, coordinated-N atoms, and the *CO/*COOH intermediates. This observation strongly suggests that the incorporation of Ni-Ag dual-atom pairs enhances the stabilization of *CO/*COOH adsorption and effectively reduces the energy barrier associated with the overall process.

Moreover, the free energy diagrams for ECO₂R yielding CO and the corresponding adsorption modes are revealed to evaluate the selectivity and reactivity in a specific manner. According to Fig. 6c, the formation of *COOH species in the ECO₂R-to-CO steps is found to be an endothermic process with energy barriers of 0.64 eV, 0.78 eV, and 1.63 eV for N₃-Ni*-Ag-N₃, Ni-N₃, and Ag-N₃, separately. This is consistent with the Tafel results, which indicates that the *COOH formation step is the rate-determining step. The heteronuclear Ni-Ag dual-atom sites in Ni-Ag/PC-N decrease the energy barrier by 0.14 eV and 0.99 eV compared to Ni-N₃ and Ag-N₃, resulting in higher catalytic activity. Ni-Ag/PC-N exhibits the lowest adsorption energy for *COOH species. The affinity of CO species towards Ag/PC-N is notably the lowest, and it exhibits a decreasing trend from Ni-Ag/PC-N to Ni/PC-N, which aligns perfectly with the results derived from the difference in charge density (Fig. 6b). The electron selectivity of the HER and ECO₂R, can be quantified by $U_L(\text{CO}_2) - U_L(\text{H}_2)$ values, whereas $U_L(\text{CO}_2)$ and $U_L(\text{H}_2)$ denote the theoretical limiting potentials of ECO₂R and HER ($U_L = -\Delta G_0/e$), respectively (Fig. 6d and S19) [14,58,59]. The $U_L(\text{CO}_2) - U_L(\text{H}_2)$ values are highest for Ni-Ag/PC-N (0.507 V), followed by Ag/PC-N (0.035 V) and Ni/PC-N (0.008 V). Among the single-atom counterparts (i.e., Ni/PC-N and Ag/PC-N), the N₃-Ni*-Ag-N₃ neighboring site shows the most positive $U_L(\text{CO}_2) - U_L(\text{H}_2)$ value. These computational findings suggest that Ni-Ag/PC-N exhibits the best inhibition of HER and the highest selectivity towards ECO₂R, which aligns with experimental observations such as FEs, ECSA, and OH⁻ adsorption tests.

In order to gain a deeper understanding of the interactions between the reaction intermediates (*COOH/*CO) and the synergistic Ni-Ag/PC-N sites, the projected densities of states (pDOS) for the Ni-3d, Ag-3d, and C-2p orbitals among the Ni-Ag/PC-N, Ni/PC-N and Ag/PC-N were computed and analyzed. The results depicted in Fig. 6e and f reveal clear hybridization between the Ni-3d, Ag-3d, and C-2p orbitals (originating from *COOH and *CO) among the simulated models, signifying the presence of strong binding interactions within the coordination environment. Notably, in contrast to the mononuclear counterparts (Ni: -2.16 eV and Ag: -2.86 eV), the d-band center of Ni in the heterodiatom Ni-Ag/PC-N adsorbed *COOH (-1.41 eV) approaches the Fermi level ($E_f = 0$ eV) more closely. This can be attributed to the redistribution of charges induced in the Ni-Ag/PC-N model after the introduction of Ag species, resulting in the narrowing of the d-band gap of the Ni species in N₃-Ni*-Ag-N₃ and thus enhancing the electron mobility and accelerating the formation of *COOH [48]. However, the d-band center of Ni in Ni-Ag/PC-N adsorbed *CO decreases from -1.20 eV to -1.59 eV compared to Ni/PC-N adsorbed *CO, indicating a weakened capability for electron transfer. This suggests a lower binding affinity of the *CO intermediate at the N₃-Ni*-Ag-N₃ site and a reduced resistance to CO molecule desorption, which is in close agreement with both the charge density difference and the free energy calculations [21,60].

Based on the theoretical calculations, it has been determined that Ni/Ag dual-atom catalysts outperform their single-atom counterparts (i.e., Ni/PC-N and Ag/PC-N) in ECO₂R-to-CO. The synergistic effects of the heteronuclear Ni-Ag dual-atom pairs have been explained in detail from a thermodynamic perspective. When compared to Ni-N₃, the introduction of neighboring Ag atoms eliminates the strong *CO affinity-induced poisoning effect on Ni atomic sites, as well as the limitations of the CO desorption step. Further, the inclusion of neighboring Ni atoms significantly reduces the energy barrier for the formation of the crucial intermediate *COOH compared to Ag atomic sites.

4. Conclusions

To summarize, we have successfully fabricated a superb Ni-Ag/PC-N electrocatalyst by the cascade-anchored pyrolysis method, which incorporates a layered porous and defective carbon matrix with heteronuclear Ni-Ag dual-atom sites. When tested in a 0.1 M aqueous KHCO₃ solution, the Ni-Ag/PC-N exhibits remarkable reactivity in CO production. It achieves a high FE_{CO} of 99.2% at -0.8 V vs. RHE and maintains a FE over 90% within a wider applied potential window of -0.7 to -1.3 V vs. RHE. Furthermore, experimental evidence confirms that the synergistic Ni-Ag dual-atom sites in the Ni-Ag/PC-N catalyst promote the physical adsorption of CO₂ molecules and stabilize bicarbonate species *CO₂⁻. In-depth analyses using *in situ* FTIR and Raman spectroscopy reveal that *COOH radicals are of paramount importance as key intermediates, further confirming that the conversion of *CO₂⁻ to *COOH is the rate-determining step in the ECO₂R-to-CO process, aligns with the insights gained from Tafel curve analysis. Theoretical calculations using DFT further support the notion that the construction of Ni-Ag dual-atom pairs addresses some intrinsic issues of Ni-/Ag-SACs, such as reducing the affinity of *CO to Ni atoms and lowering the adsorption energy barrier of *COOH to Ag atoms. This study establishes a general synthesis pathway for the symbiotic formation of heteronuclear dual-atom sites, which can greatly enhance the ECO₂R process. Furthermore, the combination of electrochemical experiments, *in situ* spectroscopy, and DFT calculations provide a comprehensive approach for understanding the synergistic effect within DACs and exploring the structure-function relationship between DACs and ECO₂R.

CRedit authorship contribution statement

Zeyu Guo: Conceptualization, Methodology, Investigation, Formal analysis, Writing – original draft. **Huiwen Zhu:** Data curation, Validation. **Gang Yang:** Formal analysis, Data curation. **Angjian Wu:** Formal analysis. **Quhan Chen:** Investigation, Data curation. **Zijun Yan:** Formal analysis, Data curation. **Kam Loon Fow:** Supervision, Writing – review & editing. **Hainam Do:** Supervision, Writing – review & editing. **Jonathan D. Hirst:** Supervision, Writing – review & editing. **Tao Wu:** Funding acquisition, Project administration, Resources. **Mengxia Xu:** Supervision, Writing – review & editing, Funding acquisition.

Declaration of Competing Interest

The authors declare that they have no known competing financial interests or personal relationships that could have appeared to influence the work reported in this paper.

Data availability

Data will be made available on request.

Acknowledgments

This work is supported by Zhejiang Provincial Department of Science and Technology under its Provincial Key Laboratory Program (2020E10018). A.W. expresses gratitude for the financial support received from the Pioneer R&D Program of Zhejiang Province (2022C03040). J.D.H is supported by the Royal Academy of Engineering under the Chairs in Emerging Technologies scheme (CiET2021_17). Z.G. acknowledges the University of Nottingham Ningbo China for providing a full PhD scholarship.

Appendix A. Supplementary data

Supplementary data to this article can be found online at <https://doi.org/10.1016/j.cej.2023.146556>.

References

- [1] A. Majumdar, J. Deutch, Research opportunities for CO₂ utilization and negative emissions at the gigatonne scale, *Joule* 2 (2018) 805–809, <https://doi.org/10.1016/j.joule.2018.04.018>.
- [2] R.G. Grim, Z. Huang, M.T. Guarnieri, J.R. Ferrell, L. Tao, J.A. Schaidle, Transforming the carbon economy: Challenges and opportunities in the convergence of low-cost electricity and reductive CO₂ utilization, *Energy Environ. Sci.* 13 (2020) 472–494, <https://doi.org/10.1039/c9ee02410g>.
- [3] Y.Y. Birdja, E. Pérez-Gallent, M.C. Figueiredo, A.J. Göttle, F. Calle-Vallejo, M.T. M. Koper, Advances and challenges in understanding the electrocatalytic conversion of carbon dioxide to fuels, *Nat. Energy* 4 (2019) 732–745, <https://doi.org/10.1038/s41560-019-0450-y>.
- [4] P. De Luna, C. Hahn, D. Higgins, S.A. Jaffer, T.F. Jaramillo, E.H. Sargent, What would it take for renewably powered electrosynthesis to displace petrochemical processes? *Science* 364 (2019) eaav3506, <https://doi.org/10.1126/science.aav3506>.
- [5] S. Banerjee, C.S. Gerke, V.S. Thoi, Guiding CO₂RR selectivity by compositional tuning in the electrochemical double layer, *Acc. Chem. Res.* 55 (2022) 504–515, <https://doi.org/10.1021/acs.accounts.1c00680>.
- [6] P. Saha, S. Amanullah, A. Dey, Selectivity in electrochemical CO₂ reduction, *Acc. Chem. Res.* 55 (2022) 134–144, <https://doi.org/10.1021/acs.accounts.1c00678>.
- [7] H.B. Yang, S.-F. Hung, S. Liu, K. Yuan, S. Miao, L. Zhang, X. Huang, H.-Y. Wang, W. Cai, R. Chen, J. Gao, X. Yang, W. Chen, Y. Huang, H.M. Chen, C.M. Li, T. Zhang, B. Liu, Atomically dispersed Ni(I) as the active site for electrochemical CO₂ reduction, *Nat. Energy* 3 (2018) 140–147, <https://doi.org/10.1038/s41560-017-0078-8>.
- [8] S. Gao, Y. Lin, X. Jiao, Y. Sun, Q. Luo, W. Zhang, D. Li, J. Yang, Y. Xie, Partially oxidized atomic cobalt layers for carbon dioxide electroreduction to liquid fuel, *Nature* 529 (2016) 68–71, <https://doi.org/10.1038/nature16455>.
- [9] Z. Zhu, Z. Li, J. Wang, R. Li, H. Chen, Y. Li, J.S. Chen, R. Wu, Z. Wei, Improving NiN_x and pyridinic N active sites with space-confined pyrolysis for effective CO₂ electroreduction, *eScience*, 2 (2022) 445–452. <https://doi.org/10.1016/j.esci.2022.05.002>.
- [10] L. Liu, A. Corma, Metal catalysts for heterogeneous catalysis: from single atoms to nanoclusters and nanoparticles, *Chem. Rev.* 118 (2018) 4981–5079, <https://doi.org/10.1021/acs.chemrev.7b00776>.
- [11] T. Tang, Z. Wang, J. Guan, Optimizing the electrocatalytic selectivity of carbon dioxide reduction reaction by regulating the electronic structure of single-atom M-N-C materials, *Adv. Funct. Mater.* 32 (2022) 2111504, <https://doi.org/10.1002/adfm.202111504>.
- [12] S.K. Kaiser, Z. Chen, D. Faust Akl, S. Mitchell, J. Pérez-Ramírez, Single-atom catalysts across the periodic table, *Chem. Rev.* 120 (2020) 11703–11809, <https://doi.org/10.1021/acs.chemrev.0c00576>.
- [13] Y. Gao, B. Liu, D. Wang, Microenvironment engineering of single/dual-atom catalysts for electrocatalytic application, *Adv. Mater.*, N/a (2023) 2209654, <https://doi.org/10.1002/adma.202209654>.
- [14] H. Cheng, X. Wu, M. Feng, X. Li, G. Lei, Z. Fan, D. Pan, F. Cui, G. He, Atomically dispersed Ni/Cu dual sites for boosting the CO₂ reduction reaction, *ACS Catal.* 11 (2021) 12673–12681, <https://doi.org/10.1021/acscatal.1c02319>.
- [15] M. Feng, X. Wu, H. Cheng, Z. Fan, X. Li, F. Cui, S. Fan, Y. Dai, G. Lei, G. He, Well-defined Fe–Cu diatomic sites for efficient catalysis of CO₂ electroreduction, *J. Mater. Chem. A* 9 (2021) 23817–23827, <https://doi.org/10.1039/d1ta02833b>.
- [16] T. He, A.R.P. Santiago, Y. Kong, M.A. Ahsan, R. Luque, A. Du, H. Pan, Atomically dispersed heteronuclear dual-atom catalysts: a new rising star in atomic catalysis, *Small* 18 (2022) 2106091, <https://doi.org/10.1002/sml.202106091>.
- [17] L. Jiao, J. Zhu, Y. Zhang, W. Yang, S. Zhou, A. Li, C. Xie, X. Zheng, W. Zhou, S.-H. Yu, H.-L. Jiang, Non-bonding interaction of neighboring Fe and Ni single-atom pairs on MOF-derived N-doped carbon for enhanced CO₂ electroreduction, *J. Am. Chem. Soc.* 143 (2021) 19417–19424, <https://doi.org/10.1021/jacs.1c08050>.
- [18] J.J. Kas, F.D. Vila, C.D. Pemmaraju, T.S. Tan, J.J. Rehr, Advanced calculations of X-ray spectroscopies with FEFF10 and Corvus, *J. Synchrotron Radiat.* 28 (2021) 1801–1810, <https://doi.org/10.1107/S1600577521008614>.
- [19] J. Pei, T. Wang, R. Sui, X. Zhang, D. Zhou, F. Qin, X. Zhao, Q. Liu, W. Yan, J. Dong, L. Zheng, A. Li, J. Mao, W. Zhu, W. Chen, Z. Zhuang, N-Bridged Co–Ni: new bimetallic sites for promoting electrochemical CO₂ reduction, *Energy Environ. Sci.* 14 (2021) 3019–3028, <https://doi.org/10.1039/d0ee03947k>.
- [20] W. Ren, X. Tan, W. Yang, C. Jia, S. Xu, K. Wang, S.C. Smith, C. Zhao, Isolated diatomic Ni-Fe metal-nitrogen sites for synergistic electroreduction of CO₂, *Angew. Chem. Int. Ed.* 58 (2019) 6972–6976, <https://doi.org/10.1002/anie.201901575>.
- [21] Y. Wang, B.J. Park, V.K. Paidi, R. Huang, Y. Lee, K.-J. Noh, K.-S. Lee, J.W. Han, Precisely constructing orbital coupling-modulated dual-atom Fe pair sites for synergistic CO₂ electroreduction, *ACS Energy Lett.* 7 (2022) 640–649, <https://doi.org/10.1021/acsenergylett.1c02446>.
- [22] H. Guo, D.-H. Si, H.-J. Zhu, Q.-X. Li, Y.-B. Huang, R. Cao, Ni single-atom sites supported on carbon aerogel for highly efficient electroreduction of carbon dioxide with industrial current densities, *eScience*, 2 (2022) 295–303. <https://doi.org/10.1016/j.esci.2022.03.007>.
- [23] K. Jiang, S. Siahrostami, T. Zheng, Y. Hu, S. Hwang, E. Stavitski, Y. Peng, J. Dynes, M. Gangisetty, D. Su, K. Attenkofer, H. Wang, Isolated Ni single atoms in graphene nanosheets for high-performance CO₂ reduction, *Energy Environ. Sci.* 11 (2018) 893–903, <https://doi.org/10.1039/c7ee03245e>.
- [24] X. Rong, H.-J. Wang, X.-L. Lu, R. Si, T.-B. Lu, Controlled synthesis of a vacancy-defect single-atom catalyst for boosting CO₂ electroreduction, *Angew. Chem. Int. Ed.* 59 (2020) 1961–1965, <https://doi.org/10.1002/ange.201912458>.
- [25] P. Lu, Y. Yang, J. Yao, M. Wang, S. Dipazir, M. Yuan, J. Zhang, X. Wang, Z. Xie, G. Zhang, Facile synthesis of single-nickel-atomic dispersed N-doped carbon framework for efficient electrochemical CO₂ reduction, *Appl. Catal. B* 241 (2019) 113–119, <https://doi.org/10.1016/j.apcatb.2018.09.025>.
- [26] X. Yang, J. Cheng, B. Fang, X. Xuan, N. Liu, X. Yang, J. Zhou, Single Ni atoms with higher positive charges induced by hydroxyls for electrocatalytic CO₂ reduction, *Nanoscale* 12 (2020) 18437–18445, <https://doi.org/10.1039/d0nr04391e>.
- [27] C. Zhao, X. Dai, T. Yao, W. Chen, X. Wang, J. Wang, J. Yang, S. Wei, Y. Wu, Y. Li, Ionic exchange of metal-organic frameworks to access single nickel sites for efficient electroreduction of CO₂, *J. Am. Chem. Soc.* 139 (2017) 8078–8081, <https://doi.org/10.1021/jacs.7b02736>.
- [28] W. Ju, A. Bagger, G.-P. Hao, A.S. Varela, I. Sinev, V. Bon, B. Roldan Cuenya, S. Kaskel, J. Rossmeisl, P. Strasser, Understanding activity and selectivity of metal-nitrogen-doped carbon catalysts for electrochemical reduction of CO₂, *Nat. Commun.* 8 (2017) 944, <https://doi.org/10.1038/s41467-017-01035-z>.
- [29] S. Liu, H. Tao, L. Zeng, Q. Liu, Z. Xu, Q. Liu, J.-L. Luo, Shape-dependent electrocatalytic reduction of CO₂ to CO on triangular silver nanoplates, *J. Am. Chem. Soc.* 139 (2017) 2160–2163, <https://doi.org/10.1021/jacs.6b12103>.
- [30] H. Mistry, Y.-W. Choi, A. Bagger, F. Scholten, C.S. Bonifacio, I. Sinev, N.J. Divins, I. Zegkinoglou, H.S. Jeon, K. Kisslinger, E.A. Stach, J.C. Yang, J. Rossmeisl, B. Roldan Cuenya, Enhanced carbon dioxide electroreduction to carbon monoxide over defect-rich plasma-activated silver catalysts, *Angew. Chem. Int. Ed.* 56 (2017) 11394–11398, <https://doi.org/10.1002/anie.201704613>.
- [31] Y. Li, C. Chen, R. Cao, Z. Pan, H. He, K. Zhou, Dual-atom Ag₂/graphene catalyst for efficient electroreduction of CO₂ to CO, *Appl. Catal. B* 268 (2020), 118747, <https://doi.org/10.1016/j.apcatb.2020.118747>.
- [32] L. Liao, G. Xia, Y. Wang, G. Ye, H. Wang, In-situ N-defect and single-metal atom synergistic engineering of high-efficiency Ag–N–C electrocatalysts for CO₂ reduction, *Appl Catal B* 318 (2022), 121826, <https://doi.org/10.1016/j.apcatb.2022.121826>.
- [33] H. Zhang, X. Jin, J.-M. Lee, X. Wang, Tailoring of active sites from single to dual atom sites for highly efficient electrocatalysis, *ACS Nano* 16 (2022) 17572–17592, <https://doi.org/10.1021/acsnano.2c06827>.
- [34] L. Liang, X. Li, J. Zhang, P. Ling, Y. Sun, C. Wang, Q. Zhang, Y. Pan, Q. Xu, J. Zhu, Y. Luo, Y. Xie, Efficient infrared light induced CO₂ reduction with nearly 100% CO selectivity enabled by metallic CoN porous atomic layers, *Nano Energy* 69 (2020), 104421, <https://doi.org/10.1016/j.nanoen.2019.104421>.
- [35] J.C.S. Wu, C.-W. Huang, In situ DRIFTS study of photocatalytic CO₂ reduction under UV irradiation, *Front. Chem. Eng. China* 4 (2010) 120–126, <https://doi.org/10.1007/s11705-009-0232-3>.
- [36] X. Cao, D. Tan, B. Wulan, K.S. Hui, K.N. Hui, J. Zhang, In situ characterization for boosting electrocatalytic carbon dioxide reduction, *Small Methods* 5 (2021) 2100700, <https://doi.org/10.1002/smt.202100700>.
- [37] Y. Zhao, X.-G. Zhang, N. Bodappa, W.-M. Yang, Q. Liang, P.M. Radjenovic, Y.-H. Wang, Y.-J. Zhang, J.-C. Dong, Z.-Q. Tian, J.-F. Li, Elucidating electrochemical CO₂ reduction reaction processes on Cu(hkl) single-crystal surfaces by in situ Raman spectroscopy, *Energy Environ. Sci.* 15 (2022) 3968–3977, <https://doi.org/10.1039/d2ee01334g>.
- [38] X. Chang, S. Vijay, Y. Zhao, N.J. Oliveira, K. Chan, B. Xu, Understanding the complementarities of surface-enhanced infrared and Raman spectroscopies in CO adsorption and electrochemical reduction, *Nat. Commun.* 13 (2022) 2656, <https://doi.org/10.1038/s41467-022-30262-2>.
- [39] I.V. Chernyshova, P. Somasundaran, S. Ponnurangam, On the origin of the elusive first intermediate of CO₂ electroreduction, *PNAS* 115 (2018) E9261–E9270, <https://doi.org/10.1073/pnas.1802256115>.
- [40] L. Zhao, Y. Zhang, L.-B. Huang, X.-Z. Liu, Q.-H. Zhang, C. He, Z.-Y. Wu, L.-J. Zhang, J. Wu, W. Yang, L. Gu, J.-S. Hu, L.-J. Wan, Cascade anchoring strategy for general mass production of high-loading single-atomic metal-nitrogen catalysts, *Nat. Commun.* 10 (2019) 1278, <https://doi.org/10.1038/s41467-019-09290-y>.
- [41] Q. Hao, H.-X. Zhong, J.-Z. Wang, K.-H. Liu, J.-M. Yan, Z.-H. Ren, N. Zhou, X. Zhao, H. Zhang, D.-X. Liu, X. Liu, L.-W. Chen, J. Luo, X.-B. Zhang, Nickel dual-atom sites for electrochemical carbon dioxide reduction, *Nat. Synth* 1 (2022) 719–728, <https://doi.org/10.1038/s44166-022-00138-w>.
- [42] Z. Pei, X.F. Lu, H. Zhang, Y. Li, D. Luan, X.W. Lou, Highly efficient electrocatalytic oxygen evolution over atomically dispersed synergistic Ni/CO dual sites, *Angew. Chem. Int. Ed.* 61 (2022) e202207537.
- [43] W. Ni, Z. Liu, Y. Zhang, C. Ma, H. Deng, S. Zhang, S. Wang, Electroreduction of carbon dioxide driven by the intrinsic defects in the carbon plane of a single Fe–N₄ site, *Adv. Mater.* 33 (2021) 2003238, <https://doi.org/10.1002/adma.202003238>.
- [44] Y. Dong, Q. Zhang, Z. Tian, B. Li, W. Yan, S. Wang, K. Jiang, J. Su, C.W. Oloman, E. L. Gyenge, R. Ge, Z. Lu, X. Ji, L. Chen, Ammonia thermal treatment toward topological defects in porous carbon for enhanced carbon dioxide electroreduction, *Adv. Mater.* 32 (2020) 2001300, <https://doi.org/10.1002/adma.202001300>.
- [45] H. Chen, X. Liang, Y. Liu, X. Ai, T. Asefa, X. Zou, Active site engineering in porous electrocatalysts, *Adv. Mater.* 32 (2020) 2002435, <https://doi.org/10.1002/adma.202002435>.
- [46] P. Yang, H. Zhuzhang, R. Wang, W. Lin, X. Wang, Carbon vacancies in a melon polymeric matrix promote photocatalytic carbon dioxide conversion, *Angew. Chem. Int. Ed.* 58 (2019) 1134–1137, <https://doi.org/10.1002/anie.201810648>.
- [47] L. Xia, Z. Sun, Y. Wu, X.-F. Yu, J. Cheng, K. Zhang, S. Sarina, H.-Y. Zhu, H. Weerathunga, L. Zhang, J. Xia, J. Yu, X. Yang, Leveraging doping and defect engineering to modulate exciton dissociation in graphitic carbon nitride for photocatalytic elimination of marine oil spill, *Chem. Eng. J.* 439 (2022), 135668, <https://doi.org/10.1016/j.cej.2022.135668>.
- [48] L. Zhao, Q. Wang, X. Zhang, C. Deng, Z. Li, Y. Lei, M. Zhu, Combined electron and structure manipulation on Fe-containing N-doped carbon nanotubes to boost

- bifunctional oxygen electrocatalysis, *ACS Appl. Mater. Interfaces* 10 (2018) 35888–35895, <https://doi.org/10.1021/acsami.8b09197>.
- [49] M. Jia, C. Choi, T.-S. Wu, C. Ma, P. Kang, H. Tao, Q. Fan, S. Hong, S. Liu, Y.-L. Soo, Y. Jung, J. Qiu, Z. Sun, Carbon-supported Ni nanoparticles for efficient CO₂ electroreduction, *Chem. Sci.* 9 (2018) 8775–8780, <https://doi.org/10.1039/C8SC03732A>.
- [50] C. Kim, H.S. Jeon, T. Eom, M.S. Jee, H. Kim, C.M. Friend, B.K. Min, Y.J. Hwang, Achieving selective and efficient electrocatalytic activity for CO₂ reduction using immobilized silver nanoparticles, *J. Am. Chem. Soc.* 137 (2015) 13844–13850, <https://doi.org/10.1021/jacs.5b06568>.
- [51] Z. Li, D. He, X. Yan, S. Dai, S. Younan, Z. Ke, X. Pan, X. Xiao, H. Wu, J. Gu, Size-dependent nickel-based electrocatalysts for selective CO₂ reduction, *Angew. Chem. Int. Ed.* 59 (2020) 18572–18577, <https://doi.org/10.1002/anie.202000318>.
- [52] M. Gattrell, N. Gupta, A. Co, A review of the aqueous electrochemical reduction of CO₂ to hydrocarbons at copper, *J. Electroanal. Chem.* 594 (2006) 1–19, <https://doi.org/10.1016/j.jelechem.2006.05.013>.
- [53] R. He, X. Yuan, P. Shao, T. Duan, W. Zhu, Hybridization of defective tin disulfide nanosheets and silver nanowires enables efficient electrochemical reduction of CO₂ into formate and syngas, *Small* 15 (2019) 1904882, <https://doi.org/10.1002/sml.201904882>.
- [54] J. Zhang, M.B. Vukmirovic, Y. Xu, M. Mavrikakis, R.R. Adzic, Controlling the catalytic activity of platinum-monolayer electrocatalysts for oxygen reduction with different substrates, *Angew. Chem. Int. Ed.* 44 (2005) 2132–2135, <https://doi.org/10.1002/anie.200462335>.
- [55] X. Wang, S. Feng, W. Lu, Y. Zhao, S. Zheng, W. Zheng, X. Sang, L. Zheng, Y. Xie, Z. Li, B. Yang, L. Lei, S. Wang, Y. Hou, A new strategy for accelerating dynamic proton transfer of electrochemical CO₂ reduction at high current densities, *Adv. Funct. Mater.* 31 (2021) 2104243, <https://doi.org/10.1002/adfm.202104243>.
- [56] M. Huang, B. Deng, X. Zhao, Z. Zhang, F. Li, K. Li, Z. Cui, L. Kong, J. Lu, F. Dong, L. Zhang, P. Chen, Template-sacrificing synthesis of well-defined asymmetrically coordinated single-atom catalysts for highly efficient CO₂ electrocatalytic reduction, *ACS Nano* 16 (2022) 2110–2119, <https://doi.org/10.1021/acsnano.1c07746>.
- [57] S. Liu, H.B. Yang, S.-F. Hung, J. Ding, W. Cai, L. Liu, J. Gao, X. Li, X. Ren, Z. Kuang, Y. Huang, T. Zhang, B. Liu, Elucidating the electrocatalytic CO₂ reduction reaction over a model single-atom nickel catalyst, *Angew. Chem. Int. Ed.* 59 (2020) 798–803, <https://doi.org/10.1002/anie.201911995>.
- [58] I. Song, Y. Eom, D.H. Hong, M. Balamurugan, R. Boppella, D.H. Kim, T.K. Kim, Geometric and electronic structural engineering of isolated Ni single atoms for a highly efficient CO₂ electroreduction, *Small* 19 (2023) 2300049, <https://doi.org/10.1002/sml.202300049>.
- [59] R. Boppella, M. Austeria, P.Y. Kim, E. Kim, I. Song, Y. Eom, D.P. Kumar, M. Balamurugan, E. Sim, D.H. Kim, T.K. Kim, Pyrrolic N-stabilized monovalent Ni single-atom electrocatalyst for efficient CO₂ reduction: Identifying the role of pyrrolic-N and synergistic electrocatalysis, *Adv. Funct. Mater.* 32 (2022) 2202351, <https://doi.org/10.1002/adfm.202202351>.
- [60] Z. Li, X. Qi, J. Wang, Z. Zhu, J. Jiang, X. Niu, A. Cabot, J.S. Chen, R. Wu, Stabilizing highly active atomically dispersed Ni₄Cl sites by Cl-doping for CO₂ electroreduction, *SusMat* 3 (2023) 498–509, <https://doi.org/10.1002/sus2.148>.